Space Weather

RESEARCH ARTICLE
10.1029/2024SW003991

Quantifying Extreme Values in Geomagnetic Perturbations Using Ground Magnetic Records

J. Rodríguez-Zuluaga[1], J. Gjerloev[1], S. Ohtani[1], Y. Zou[1], and B. Anderson[1]

[1]Johns Hopkins University Applied Physics Laboratory, Laurel, MD, USA

Key Points:

- We utilized magnetic records from about 400 stations spanning four solar cycles between 1976 and 2023 across three magnetic components
- The strongest perturbations were found in the north magnetic component associated with the dawnside westward auroral electrojet
- The weakest and most significant extreme values of perturbations were observed during ascending and declining solar phases, respectively

Supporting Information:

Supporting Information may be found in the online version of this article.

Correspondence to:

J. Rodríguez-Zuluaga,
juan.rodriguez.zuluaga@jhuapl.edu

Citation:

Rodríguez-Zuluaga, J., Gjerloev, J., Ohtani, S., Zou, Y., & Anderson, B. (2024). Quantifying extreme values in geomagnetic perturbations using ground magnetic records. *Space Weather*, *22*, e2024SW003991. https://doi.org/10.1029/2024SW003991

Received 8 MAY 2024
Accepted 8 JUL 2024

Abstract We comprehensively analyzed geomagnetic perturbations using ground magnetic records from over 400 stations spanning four solar cycles, from 1976 to 2023. We assess the perturbations in the three magnetic components separately. Our study covers low, middle, and high magnetic latitudes in the northern magnetic hemisphere, with the primary objective of quantifying extreme values and evaluating their variability on magnetic latitude, local time, and solar cycle phases "minimum, ascending, maximum, and declining." Our findings reveal spatial patterns to be less discernible as perturbations intensify, with distinct responses at middle and high latitudes. The extreme values, defined as percentiles 0 and 100, were observed to be localized and randomly distributed in local time, especially in the east magnetic component. Additionally, we observed dusk-dawn asymmetries in the magnitude of perturbations related to the auroral electrojets, indicating complex interactions between the magnetosphere and ionosphere. Furthermore, the results reveal a preference for the most significant extreme values to occur in the declining phase of the solar cycle. These insights deepen our understanding of geomagnetic perturbations and their variability, contributing to space weather forecasting and mitigation strategies.

Plain Language Summary The study aims to investigate the occurrence of geomagnetic perturbations across different regions of the Earth by analyzing data from the SuperMAG collaboration. The network records changes in Earth's magnetic field, and the study endeavors to determine the extent to which these disturbances vary across different parts of the Earth. We focused on low, middle, and high latitudes in the northern hemisphere to comprehensively understand the perturbations during their intensification. The findings of the study suggest that the behavior of the perturbations varies significantly across different regions. We observed that magnetic perturbations in the auroral region intensify more in the morning compared to the evening, indicating the dynamic interplay between Earth's magnetic field and charged particles from space. Additionally, the study discovered that as the disturbances grew stronger, they did not follow the same patterns. Instead, the disruptions varied depending on the location on Earth. Moreover, the perturbations seem to intensify more during the declining solar phase. This knowledge is crucial in predicting space weather, especially in protecting satellites and power grids from the effects of space storms.

1. Introduction

Records of the Earth's magnetic field are described as a superposition of several sources from which electric currents in the outer core represent the largest source with several tens of thousands of nanoteslas measured on the Earth's surface. Although all the other sources together account for only a few percent of the magnetic field, some of them can still cause significant space weather events. It is well established that ground-based magnetic records display perturbations on the order of tens to thousands of nanoteslas caused by electric currents flowing in the upper atmosphere (e.g., Kamide et al., 1981). From all the currents in the ionosphere, magnetosphere, and magnetopause, the majority of geomagnetic perturbations recorded on ground can be attributed to field-aligned currents, auroral and equatorial electrojets, and solar quiet currents. During storm time, however, additional currents such as the ring current and Chapman-Ferraro current play a significant role as well.

In the auroral region, electric currents are arranged in a configuration consisting of downward and upward field-aligned current (FAC) sheets that are connected in the ionosphere through meridional Pedersen currents, while divergence-free Hall currents flow azimuthally. Following Iijima and Potemra (1976), there are two sets of FAC, namely region-1 current (R1-FAC) and region-2 current (R2-FAC), that flow at different latitudes, as depicted in Figure 1a. In the dusk sector, the downward R2-FAC feeds an upward R1-FAC, and the meridional electric field points poleward. In the dawn sector, the electric field points equatorward, and the direction of the two FACs

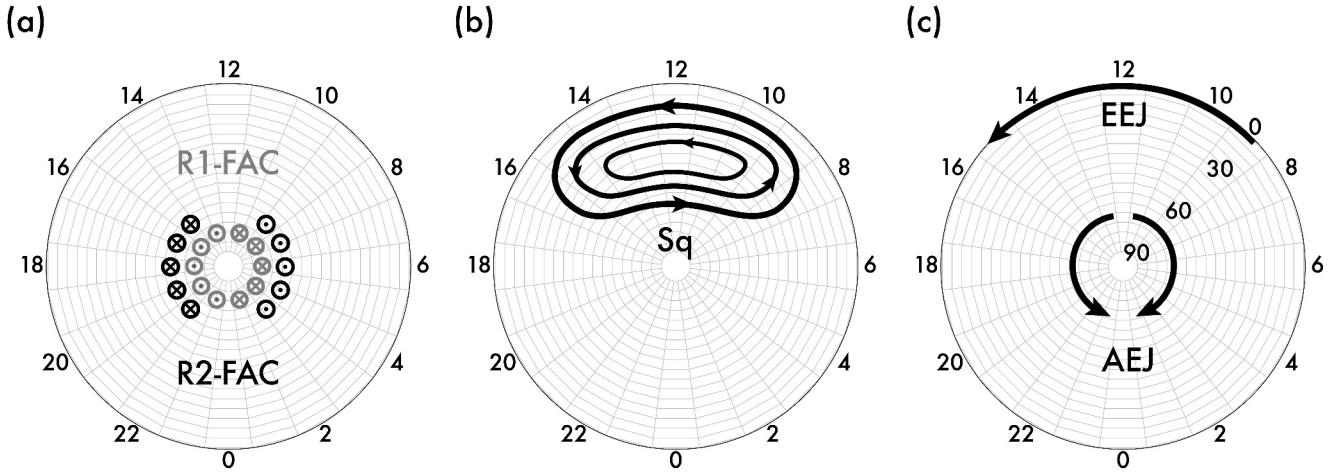

Figure 1. Polar maps depicting the northern magnetic hemisphere in terms of local time and latitude, illustrating sketches of (a) the region-1 field-aligned currents (R1-FAC) and region-2 field-aligned currents (R2-FAC), (b) the solar quiet current system (Sq), and (c) the auroral electrojet (AEJ) and equatorial electrojet (EEJ).

reverses. Additionally, the meridional electric field drives a Hall current known as the auroral electrojet (AEJ), which flows toward the east in the dusk sector and toward the west in the dawn sector, as shown in Figure 1c. A concise review of ionospheric and field-aligned currents in the auroral zone is given by Baumjohann (1982).

At middle and low magnetic latitudes, the solar quiet (Sq) currents are responsible for most of the regular daily variation of the geomagnetic field due to its dependence on solar time. The Sq current system consists of a large-scale counter-clockwise vortex on the dayside of the northern hemisphere (see Figure 1b), and a large-scale clockwise vortex on the dayside of the southern hemisphere. At the dip equator, the Sq current vortices of the southern and northern hemispheres touch each other and form an extended nearly jet-like zonally eastward current, namely the equatorial electrojet (EEJ), as depicted by Figure 1c. However, the existence of the EEJ is not completely explained by the convergence of both Sq vortices. The combination of the magnetic field parallel to the Earth's surface at the dip equator and the nearly perpendicular incidence of solar radiation causes an enhancement in the effective conductivity, which leads to an amplification of the current. For a thorough understanding of both Sq current system and EEJ, the reader is pointed to the review papers by Yamazaki and Maute (2017) and Lühr et al. (2021).

Geomagnetic perturbations can be induced by several external events, including solar flares, coronal mass ejections (CME), and other space weather phenomena. Geomagnetic storms are among the most severe examples of these disturbances, and they occur when the Earth's magnetic field is quickly compressed and twisted by the incoming solar wind. Extreme geomagnetic storms can be highly disruptive, potentially resulting in satellite failures, power outages, and other broad effects that jeopardize public safety and inflict significant economic losses (e.g., Baker et al., 2013; Cliver & Svalgaard, 2004; Lanzerotti, 2017). Over the last few decades, research has been conducted on the frequency and magnitude of extreme space weather events, as well as their associated geomagnetic perturbations. A variety of statistical methods have been developed to examine historical data and estimate the likelihood of extreme events occurring in the future (e.g., Bergin et al., 2023; Koons, 2001; Love et al., 2015; Riley, 2018; Tsubouchi & Omura, 2007). The results have shown that extreme geomagnetic storms are unusual events, but their impact can be severe, and the possibility of such events occurring is higher than previously anticipated (Pulkkinen et al., 2011; Riley & Love, 2017). In this regard, the correlation between the occurrence of extreme geomagnetic storms and the solar cycle characteristics, such as its strength and phase, is not completely understood. Studies of this nature usually use geomagnetic indexes such as *Dst*, *ap*, or *aa* to assess the possible connection between geomagnetic activity and solar cycle (e.g., Hathaway, 2015; Kilpua et al., 2015; Legrand & Simon, 1989; Reyes et al., 2021). Kilpua et al. (2015) have shown that although the frequency of nominal geomagnetic activity varies with the strength of the solar cycle, the occurrence probability for extreme space weather does not decrease with decreasing solar cycle strength. Notably, the most extreme events show a weak correlation with the strength of the solar cycle. This observation is substantiated by the Carrington superstorm and the 2012 July extreme CME event, which occurred during relatively medium/weak-sized solar cycles. Kilpua et al. (2015) also show that the frequency of extreme events is not fully independent of the solar

cycle, as they tend to occur more often near the solar maximum. On the other hand, Hathaway (2015) has shown that based on the *aa* index and the sunspot number, geomagnetic activity tends to reach its minimum just after the sunspot number does, and it usually remains high during the declining phase of each cycle. Legrand and Simon (1989) suggest that this high level of geomagnetic activity toward the end of the cycle is caused by the impact of high-speed solar wind streams that originate from low-latitude coronal holes.

Ground magnetic records have successfully been used to map geomagnetic perturbations, revealing typical spatial patterns "i.e., magnetic local time and latitude." These patterns have been explained in terms of FAC and the auroral electrojets in polar regions (e.g., D. Weimer et al., 2010), and in terms of the Sq current system at middle latitudes (e.g., Takeda, 1999). However, most studies have focused on average values using a few stations and spherical harmonics analysis. In this study, we use magnetic records from the extensive multi-year data set provided by the SuperMAG collaboration to comprehensively analyze these disturbances separately in the three magnetic components. The magnetic records come from roughly 400 stations in the northern magnetic hemisphere expanding over four solar cycles from 1976 to 2023. We examine their dependence on magnetic latitude and local time, covering low, middle, and high magnetic latitudes in the northern hemisphere, where the largest and oldest data sets are available. Our primary goal is to quantify extreme values and evaluate their variability on magnetic latitude and local time. We also focus our study on how the geomagnetic perturbations and their spatial patterns and intensities vary along different solar cycle phases.

2. Data Set and Processing

This study uses ground-based vector magnetic field measurements from the SuperMag collaboration available from 1976 to 2023 covering almost four solar cycles. SuperMAG is a global partnership of ground-based magnetometers that measure variations in the Earth's magnetic field. The network currently consists of about 400 magnetometers covering the majority of the northern hemisphere (Figure 2a). We use the entire data set from 1976 to 2023 providing a good coverage, as it is displayed by Figure 2b. It is a matter of concern that the analysis is limited to only the northern hemisphere, as it omits an entire hemisphere that could have different dynamics. However, this decision is based on the fact that there are many stations with long-term records in the northern hemisphere, making the spatial distribution of data more extensive and reliable. The SuperMAG data set has been used in a wide range of studies, including investigations of substorms, magnetic reconnection, and ionospheric current systems. Its high temporal resolution and accuracy make it particularly useful for studying transient phenomena, such as geomagnetic storms and substorms, which can evolve rapidly and unpredictably.

Shortly, the SuperMAG data processing technique is a sophisticated algorithm that takes into account the varying sensitivity of the magnetometers, as well as the changing geometry of the Earth's magnetic field over time. This technique is designed to remove noise and other unwanted artifacts from the data while preserving the underlying physical signals. It involves several steps, including data cleaning, interpolation, and merging, as described in Gjerloev (2012). In this analysis, we employ 1-min temporal resolution data with the yearly-trend removed. Detailed information about the baseline determination process is found in Gjerloev (2012). The coordinate system comprises three vectors: north (N), east (E), and vertical (Z). The N-axis points to the local magnetic north, while the E-axis points to the magnetic east. The triad is completed by the Z-component pointing vertically down.

To assess geomagnetic perturbations as a function of magnetic latitude and local time, we map the disturbances in the northern magnetic hemisphere from the dip equator up to 85° of magnetic latitude. We use a grid of 1 hr of local time by five degrees of magnetic latitude. Our analysis consists of using different percentiles to examine the characteristics of the perturbations in the three magnetic components as their magnitudes approach extreme values. We define extreme values as percentiles 0 (negative perturbations) and 100 (positive perturbations) for a set of magnetic records. In the polar maps, each bin shows the value of a given percentile for all the available data on a given latitude and local time bin.

3. Maps of Geomagnetic Perturbations

Ground-based magnetic field recordings provide useful insights into the complex nature of geomagnetic disturbances. Typically, their magnitudes exhibit a coherent pattern in auroral regions as they intensify and move equatorward, as shown in previous studies (e.g., D. Weimer et al., 2010; Woodroffe et al., 2016). Even though less studied, coherent patterns can also be observed at middle and low latitudes. An interesting question is whether these regular patterns prevail during extreme events. To investigate this, we analyzed data from 1976 to 2023

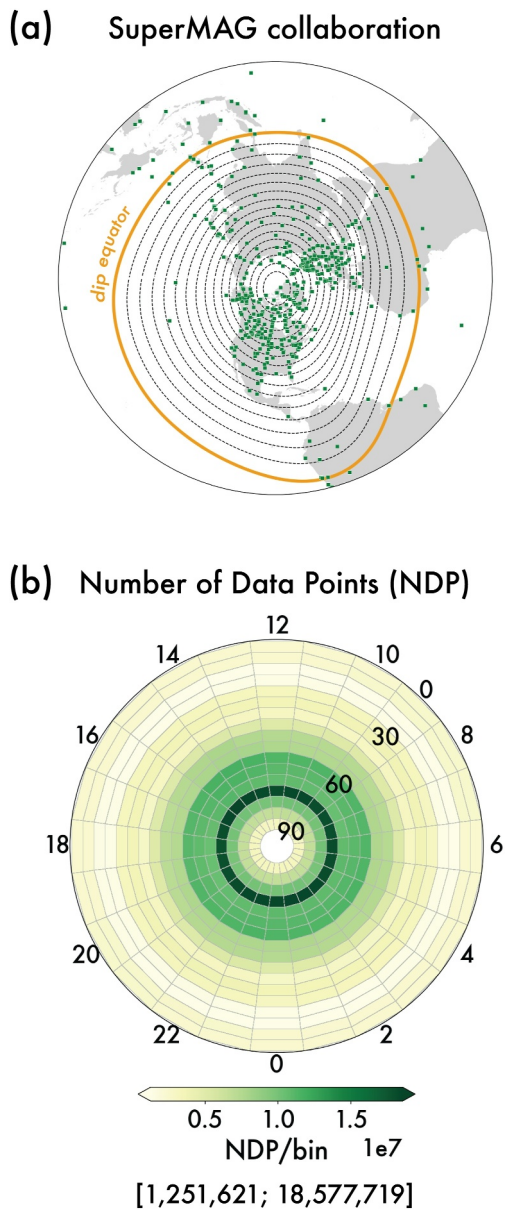

Figure 2. (a) Magnetic stations of the SuperMAG collaboration in the northern hemisphere. The yellow line depicts the dip equator. Consecutive dashed black lines are drawn every five degrees in magnetic latitude up to 85°. (b) Polar map displaying the number of data points used in this study and collected from 1976 to 2023. Each bin is part of a grid of 1 hr in magnetic local time by 5° of magnetic latitude. The number of data points corresponds to observations per bin. The minimum and maximum values are shown at the bottom of the map.

covering about four solar cycles. Subsequently, we analyze geomagnetic perturbations during minimum, ascending, maximum, and declining solar cycle phases. We use polar maps of different percentiles to consistently evaluate the spatial characteristics of the geomagnetic perturbations, focusing on the 0 and 100 percentiles to assess the patterns during extreme values. In this regard, after a visual inspection of different percentiles, we have strategically shown in this study, percentile 50 ($\mathbf{P_{50}}$) to show the regular patterns of geomagnetic perturbations, percentiles 1 and 99 ($\mathbf{P_1}$ and $\mathbf{P_{99}}$) to depict the evolution of the perturbations as their magnitude increases, percentiles 0.001 and 99.999 ($\mathbf{P_{0.001}}$ and $\mathbf{P_{99.999}}$) to illustrate the point at which patterns in geomagnetic perturbations become less discernible at middle latitudes, and percentiles 0.0001 and 99.9999 ($\mathbf{P_{0.0001}}$ and $\mathbf{P_{99.9999}}$) to spot such change in the auroral zone. The percentiles at which the regular patterns become indistinct have been identified by visual inspection. Finally, we present percentiles 0 and 100 to illustrate the extreme values for the entire data set.

3.1. Spatial Patterns

In Figure 3, we examine the 50th percentile using the SuperMAG data set from 1976 to 2023. The figure includes three polar maps, each representing one of the three magnetic components. The maps displayed the value of the percentiles using a logarithmically normalized color scale. We normalized the color scale of each map to use a single color bar for all the polar plots. The normalization is done separately for each map based on the maximum bin value. To indicate the range of variability, the upper left corner of each map indicates the minimum and maximum values. Since the magnitude of geomagnetic disturbances can vary significantly between the auroral region and middle latitudes, a logarithmic scale is used in the figure to highlight the values in the middle more effectively.

Upon initial examination, the maps show common trends in the perturbations that were documented in previous studies (e.g., Takeda, 1999; D. R. Weimer, 2013; Yamazaki & Maute, 2017). By following the diagrams in Figure 1 and using the right-hand rule, it is fair to say that Figure 3 displays clear signatures of eastward (blue) and westward (red) auroral electrojets (AEJ). The perturbations associated with AEJ are evident in both north and vertical magnetic components, $\mathbf{dB_N}$ and $\mathbf{dB_Z}$, centered at about the dusk and dawn sectors, above approximately 65° of magnetic latitude. At middle and equatorial latitudes, the three magnetic components show the Sq current system and the equatorial electrojet (EEJ) on the daytime side, with the latter exhibiting the highest median values of approximately 66 nT in $\mathbf{dB_N}$ around noon. In the midnight sector, $\mathbf{dB_N}$ is mainly negative below 65°, indicating westward zonal currents, with slightly higher values below 30° in the midnight-dusk sector. The eastern magnetic component, $\mathbf{dB_E}$, provides evidence of downward and upward field-aligned currents (FAC) above roughly 70°. At middle and low latitudes, the day side of $\mathbf{dB_E}$ displays opposite patterns related to the Sq current system. At around 11 MLT, the sign of the perturbations changes, indicating the location of the Sq focus, consistent with previous studies (e.g., Yamazaki & Maute, 2017, and references therein). Although less intense, this opposing pattern extends to the night sector, particularly at middle latitudes. Above 65°, the vertical magnetic component, $\mathbf{dB_Z}$, is generally associated with the AEJ. At middle and low latitudes, the negative $\mathbf{dB_Z}$ on the day side comes mainly from the Sq current system.

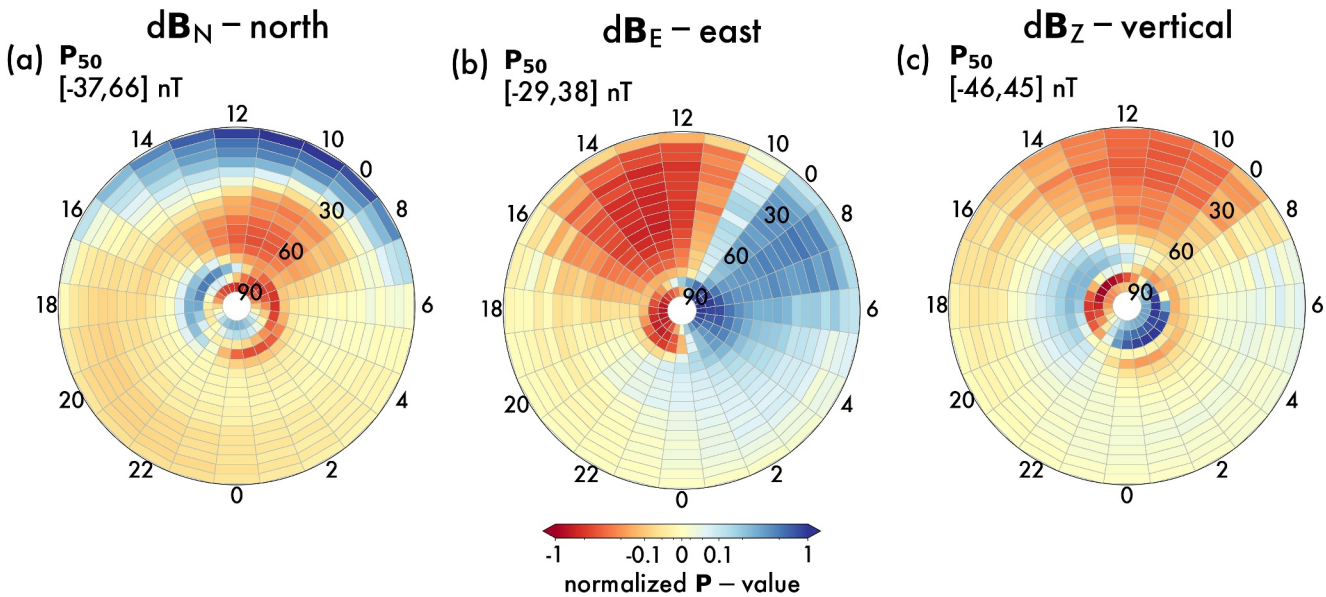

Figure 3. Polar maps of the 50th percentile ($\mathbf{P_{50}}$) of geomagnetic perturbations from 1976 to 2023. Each magnetic component is depicted separately as a function of magnetic local time and magnetic latitude (a) north $\mathbf{dB_N}$, (b) east $\mathbf{dB_E}$, and (c) vertical $\mathbf{dB_Z}$. Each polar map covers the northern magnetic hemisphere. Each pixel is part of a grid of 1 hr in magnetic local time by 5° of magnetic latitude. The color scale is normalized by the maximum value of each polar map and displayed logarithmically. To indicate the range of variability, both minimum and maximum values are displayed in the left upper corner of each map.

3.2. Toward Extreme Values

Figure 4 illustrates percentiles 1 ($\mathbf{P_1}$) "top row" and 99 ($\mathbf{P_{99}}$) "bottom row." At these percentiles, the spatial patterns remain coherent and their magnitudes increase considerably in the polar regions, compared to Figure 3. It is noteworthy that such an increase in magnitude is accompanied by a shift of the perturbations toward the equator. Upon closer examination, interesting features are visible in local time and latitude for all three components. The negative disturbances of the north component, $\mathbf{dB_N}$, "associated with the westward AEJ in the midnight-dawn sector (Figure 4a)" are almost twice the magnitude of their positive counterparts (Figure 4d). On the other hand, positive disturbances in the east component, $\mathbf{dB_E}$, are significantly amplified in the midnight-dawn sector (0–6 MLT) around 65°N (Figure 4e). At middle and low latitudes, $\mathbf{dB_E}$ still shows signatures of the Sq current system and $\mathbf{dB_N}$ of the EEJ. The latter starts to evidence a slight increase of negative perturbations (i.e., westward currents) in the dusk sector (see Figure 4a).

Percentiles 1 and 99, while interesting, occur quite frequently, happening 10 or more times a day on average. Figure 5 displays percentiles 0.001 ($\mathbf{P_{0.001}}$) "top row" and 99.999 ($\mathbf{P_{99.99}}$) "bottom row," revealing that at middle latitudes, the patterns related to Sq currents are no longer evident in all three components, while sparse and localized events become visible. Notorious negative $\mathbf{dB_N}$ perturbations occur at middle latitudes, while positive $\mathbf{dB_E}$ perturbations appear around the midnight-dusk sector at middle latitudes and a few negative in the day sector around 40°. At the dip equator, the north component $\mathbf{dB_N}$ still shows signatures of the EEJ, but westward currents start to show up importantly at the dusk sector (negative $\mathbf{dB_N}$ perturbations). In general, coherent patterns still prevail at auroral regions, although with values about four times the ones for percentiles 1 and 99, accompanied by a notorious displacement toward the equator with perturbation reaching latitudes of about 50°–45°. As a small observation, negative $\mathbf{dB_E}$ perturbations start to increase in magnitude in the dawn sector above 60°.

Figure 6 exhibits percentiles 0.0001 ($\mathbf{P_{0.0001}}$) "top row" and 99.9999 ($\mathbf{P_{99.9999}}$) "bottom row," showing how the spatial patterns in auroral regions become less distinct. Compared to the $\mathbf{dB_N}$ perturbations, $\mathbf{dB_E}$ and $\mathbf{dB_Z}$ are more randomly distributed in local time and latitude. Even though $\mathbf{dB_N}$ also exhibits localized perturbations, a local time preference is still evident. Finally, the information presented in Figure 7 sheds light on the most negative and positive values (i.e., percentiles 0 and 100) for each component, showcasing the extreme ends of the spectrum. The regular patterns are nearly indistinguishable, except for the north component, $\mathbf{dB_N}$, which maintains its preference for the midnight-dawn and noon-dusk sectors. On the other hand, $\mathbf{dB_E}$ and $\mathbf{dB_Z}$ present random and localized peaks at varying local times.

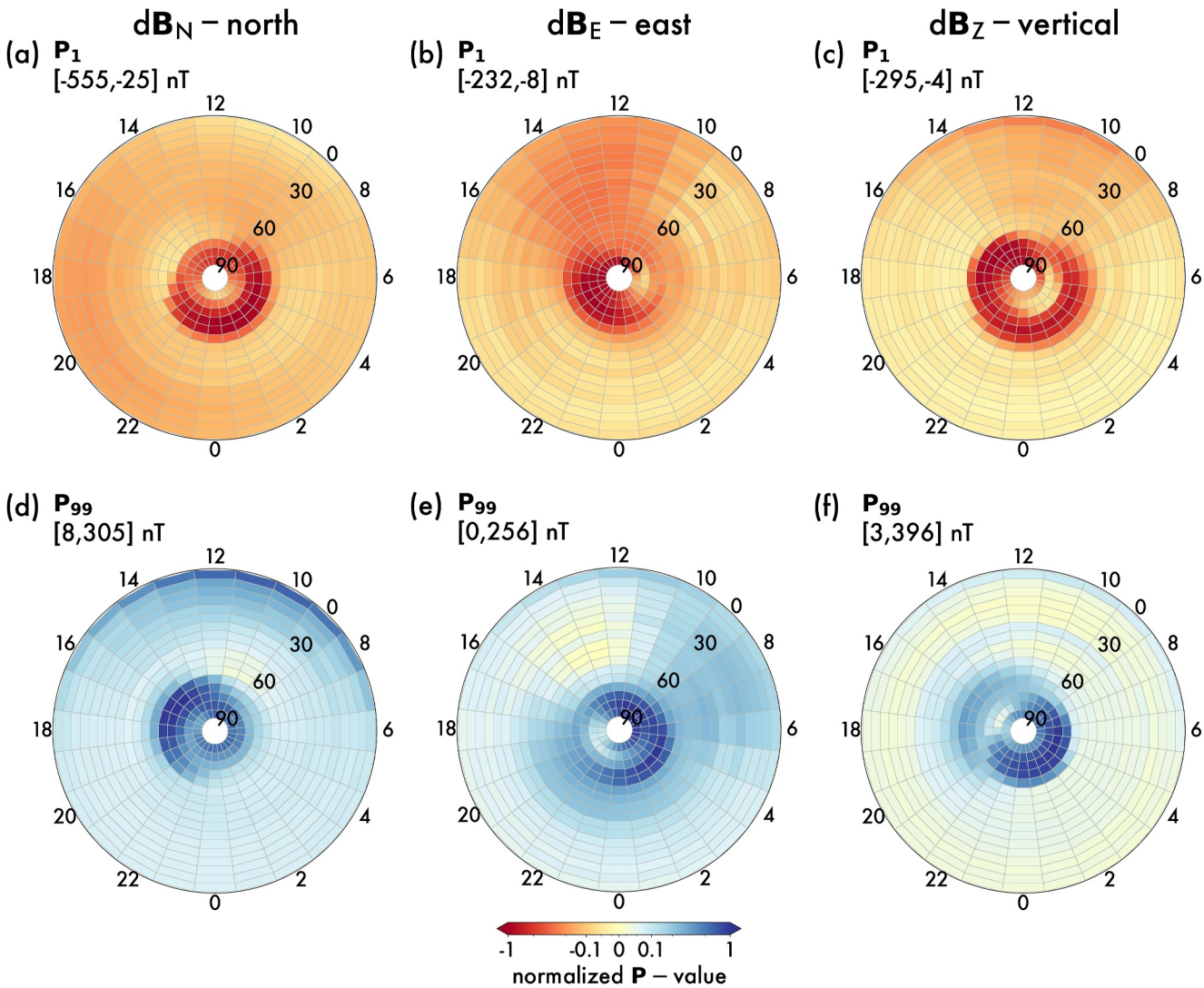

Figure 4. Polar maps of the 1st percentile ($\mathbf{P_1}$) "upper row" and 99th percentile ($\mathbf{P_{99}}$) "lower row" from 1976 to 2023. They respectively represent negative and positive disturbances as a function of magnetic local time and magnetic latitude. In the same fashion as Figure 3, each column represents each magnetic component, (a) and (d) north $\mathbf{dB_N}$, (b) and (e) east $\mathbf{dB_E}$, and (c) and (f) vertical $\mathbf{dB_Z}$. Each map covers the northern magnetic hemisphere. Each bin is part of a grid of 1 hr in magnetic local time by 5° of magnetic latitude. The color scale is normalized by the maximum value of each polar map and displayed logarithmically. To indicate the range of variability, both minimum and maximum values are displayed in the left upper corner of each map.

3.3. Solar Cycle Phases

There is a correlation between geomagnetic activity and the solar cycle, but it is more complicated than the relationship between other solar events like sunspot areas, radio flux, flares, and coronal mass ejections. The minimum level of geomagnetic activity usually occurs just after the minimum level of sunspot activity, and the level of geomagnetic activity tends to remain high during the declining phase of each cycle (Hathaway, 2015). As mentioned earlier, one of the purposes of this study is to quantify extreme values of geomagnetic perturbations. In this section, we intend to look at those extreme values by sorting the data into different solar phases and describing their characteristics. To achieve this, we have chosen the method used in the study by Getachew et al. (2017) to divide solar cycles 21, 22, 23, and 24 into four phases (minimum, ascending, maximum, and declining phases). In detail, Getachew et al. (2017) defined the date of the solar minimum to have a phase of 0° (360°) and the solar maximum at 180° for each solar cycle. They then divided the solar cycle into four phases, each with a length of 90° and linearly distributed in time. The centers of the minimum, ascending, maximum, and declining phases of the solar cycle are denoted by 0°(360°), 90°, 180°, and 270°, respectively. The ascending phase is between 45°

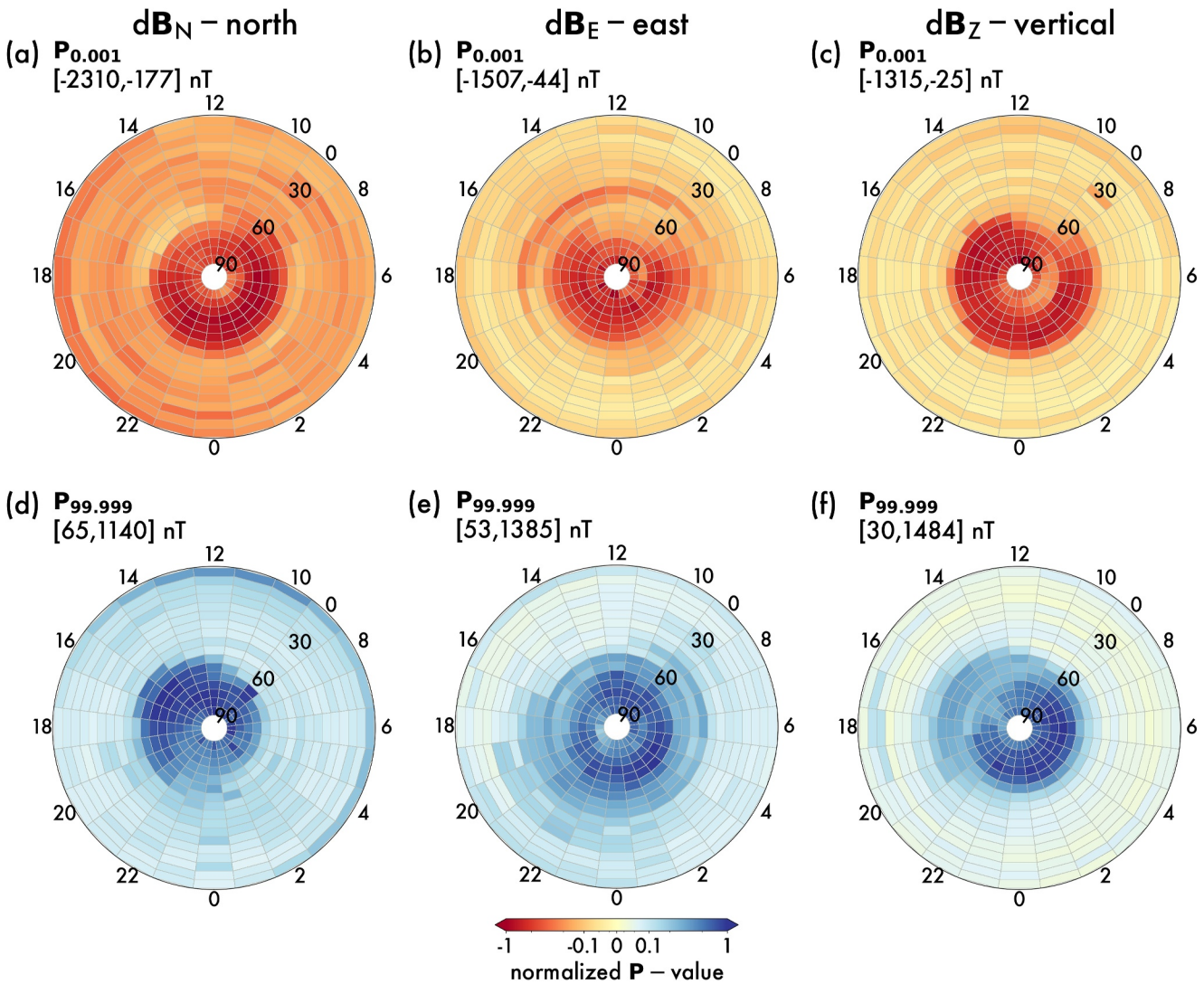

Figure 5. Same as Figure 4 for percentile 0.001 ($\mathbf{P_{0.001}}$) "upper row" and percentile 99.999 ($\mathbf{P_{99}}$) "lower row" from 1976 to 2023.

and 135°, the maximum phase is between 135° and 225°, the declining phase is between 225° and 315°, and the minimum phase is between 315° and 45°.

Figures 8–11 show percentiles 0 and 100 ($\mathbf{P_0}$ and $\mathbf{P_{100}}$ "i.e., maximum negative perturbation and maximum positive perturbation, respectively) for solar minimum, ascending, maximum, and declining phases." Negative perturbations in the north component $\mathbf{dB_N}$, which are associated with the westward AEJ, produce the strongest values during the declining phase with −4,712 nT in $\mathbf{dB_N}$, followed by the solar maximum (−3,579 nT), minimum (−3,403 nT), and ascending phase (−3,123 nT). The minimum values of negative $\mathbf{dB_N}$ perturbations, which mostly occur at middle latitudes, show a similar trend, with the most negative value being −221 nT for the declining phase and −78 nT for the minimum phase. Positive $\mathbf{dB_N}$ perturbations, which correspond to eastward AEJ, have their maximum value during the solar maximum phase (2,180 nT), followed by the declining (2,139 nT), minimum (1,618 nT), and ascending (1,384 nT) phases. The maximum values in the east component $\mathbf{dB_E}$ come from positive perturbations during the solar declining phase with 2,734 nT, followed by the maximum (2,391 nT), ascending phase (2,239 nT), and minimum (2,106 nT). The order in intensity for negative $\mathbf{dB_E}$ perturbations starts with the solar declining phase (−2,454 nT) and ends with the ascending phase (−1,573 nT). The $\mathbf{dB_Z}$ perturbations present their largest values in positive disturbances during the solar declining phase with 3,951 nT, followed by maximum (3,243 nT), minimum (2,418 nT), and ascending phase (1,856 nT). The same order in intensity occurs for negative $\mathbf{dB_Z}$ perturbations, starting with the solar declining phase (−2,411 nT) and

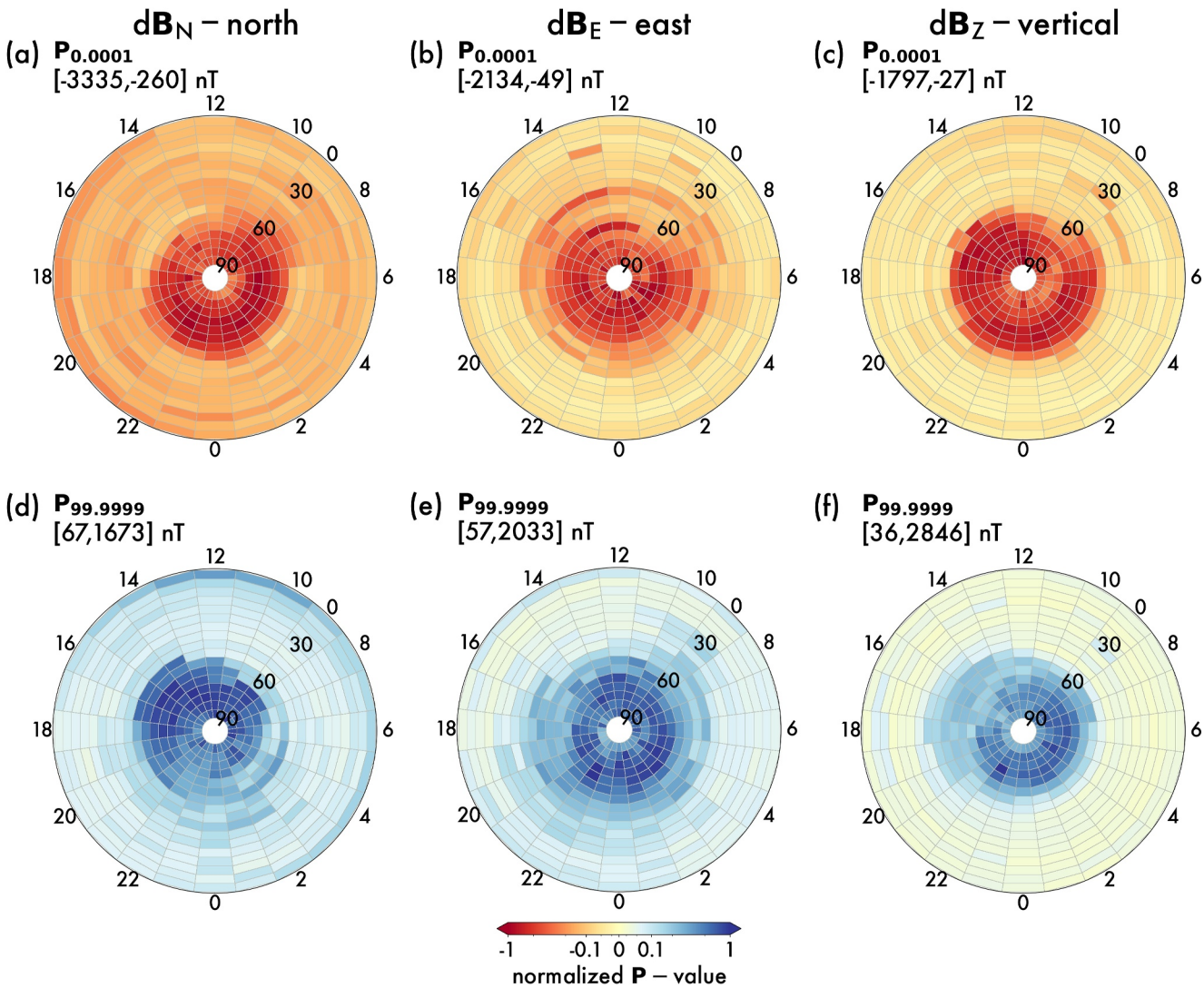

Figure 6. Same as Figure 5 for percentile 0.0001 ($\mathbf{P_{0.0001}}$) "upper row" and percentile 99.9999 ($\mathbf{P_{99.9999}}$) "lower row" from 1976 to 2023.

ending with the ascending phase (−1,637 nT). Overall, it is fair to say that the strongest perturbations mostly occur during the solar declining phase and the weakest during the solar ascending phase. Finally, we have included in the supporting material a figure (Figure S1 in Supporting Information S1) similar to Figure 2b, showing separately the number of data points per bin for the four solar phases.

4. Discussion

We use ground-based magnetic records to assess spatial characteristics of geomagnetic perturbations in the three magnetic components separately. We aim to quantify extreme values and evaluate their variability on magnetic latitude and local time using records from about 400 stations covering four solar cycles. The median of geomagnetic perturbations in Figure 3 not only evidences the good shape of the SuperMAG data but also works as evidence of what it has already been known in terms of the main electric currents from which these magnetic signatures come "i.e., field-aligned currents, auroral and equatorial electrojets, and Sq currents (see Figure 1)."

As previously noted, studies have well-documented the spatial patterns in magnetic perturbations in the auroral regions (e.g., Iijima & Potemra, 1976; Juusola et al., 2016; Kamide et al., 1981; D. Weimer, 2001). As the intensity of the perturbations increases, the magnetic records register a shift toward the equator, as Figures 4 and 5 evidence. This latitudinal displacement has been well-studied and demonstrated convincingly (e.g., Woodroffe

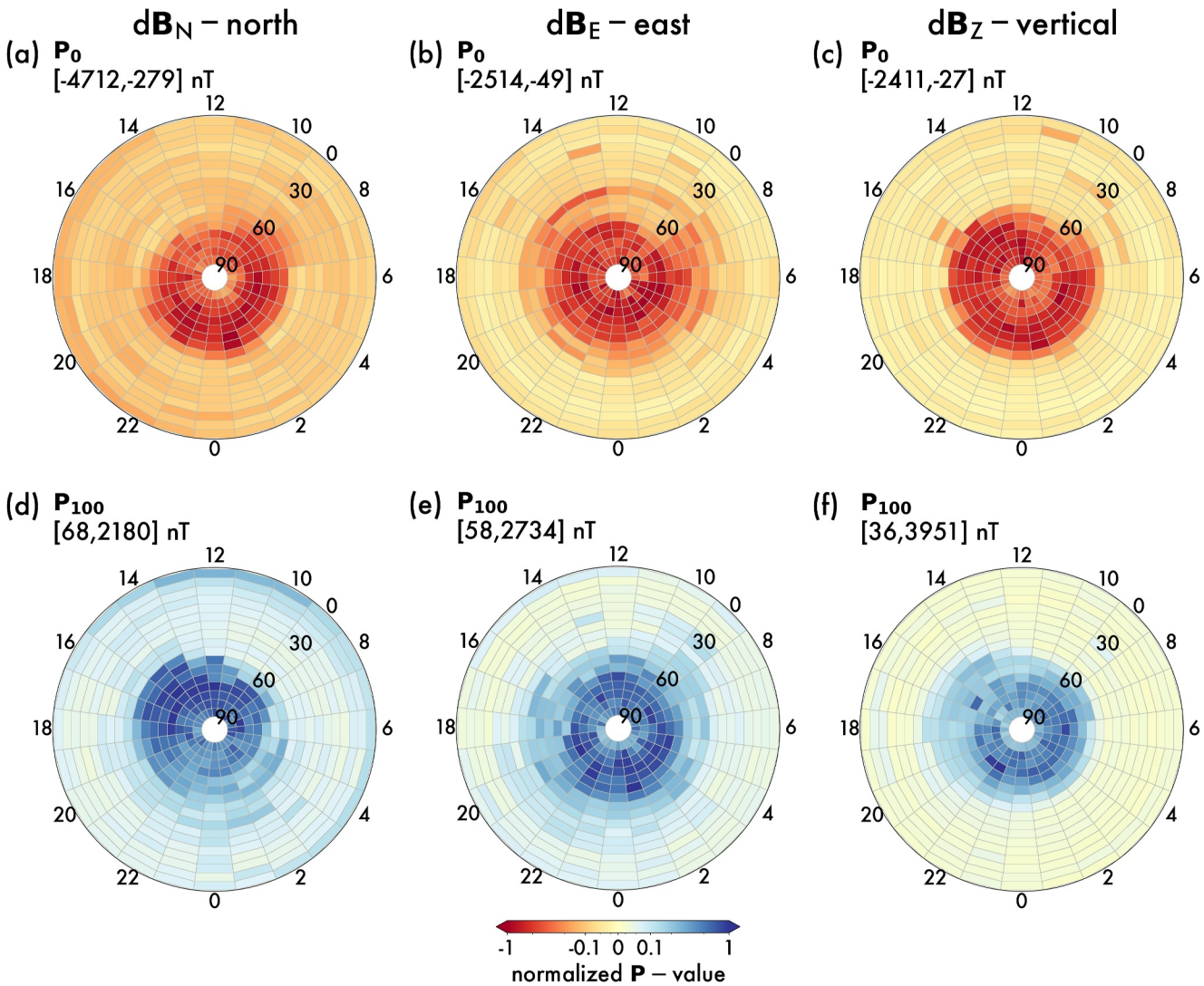

Figure 7. Same as Figure 6 for percentile 0 ($\mathbf{P_0}$) "upper row" and percentile100 ($\mathbf{P_{100}}$) "lower row" from 1976 to 2023.

et al., 2016). In addition to this common observation, an interesting phenomenon occurs on the dawn side where negative perturbations of the north component associated with the westward auroral electrojet (AEJ) double in intensity compared to their positive counterpart on the dusk side—see panels (a) and (b) of Figures 4 and 5. According to a report by Ohtani (2021), this dawn-dusk asymmetry of the AEJ is a significant attribute of the storm's main phase. In the study, the author uses SuperMAG geomagnetic indices, SMR, SMU, SML, and their sub-indices (Newell & Gjerloev, 2011, 2012). SMR is equivalent to the Sym-H index but based on data from stations in a wider range of geomagnetic latitudes. SMU and SML are equivalents to the AU and AL indices. They are the measures of the eastward and westward AEJs, respectively; more specifically, they represent the maximum intensities of the corresponding equivalent currents. Each index has four sub-indices "SMR_{hh}, SMU_{hh}, and SML_{hh}," each of which is the average of the north component measured in the magnetic local time quadrant center at *hh*: 0, 6, 12, and 18 hr (midnight, dawn, noon, and dusk). The author found that the dawn-dusk asymmetry "i.e., $\Delta SMR_{18}-\Delta SMR_6$" is better correlated with the dawnside westward AEJ (SML_6) than with its counterpart at dusk (SMU_{18}) "this latter with an insignificant correlation. Even though the magnetospheric source process could not be identified, the results suggested that the associated magnetosphere-ionosphere current system includes the dawnside westward AEJ as its ionospheric current closure. Other studies have explained this enhancement of the westward AEJ in terms of the upward R2-FAC with downstream electrons enhancing conductivity in the midnight-dawn sector (0–6 MLT) (e.g., Newell & Gjerloev, 2011; Xiong et al., 2020). In a recent

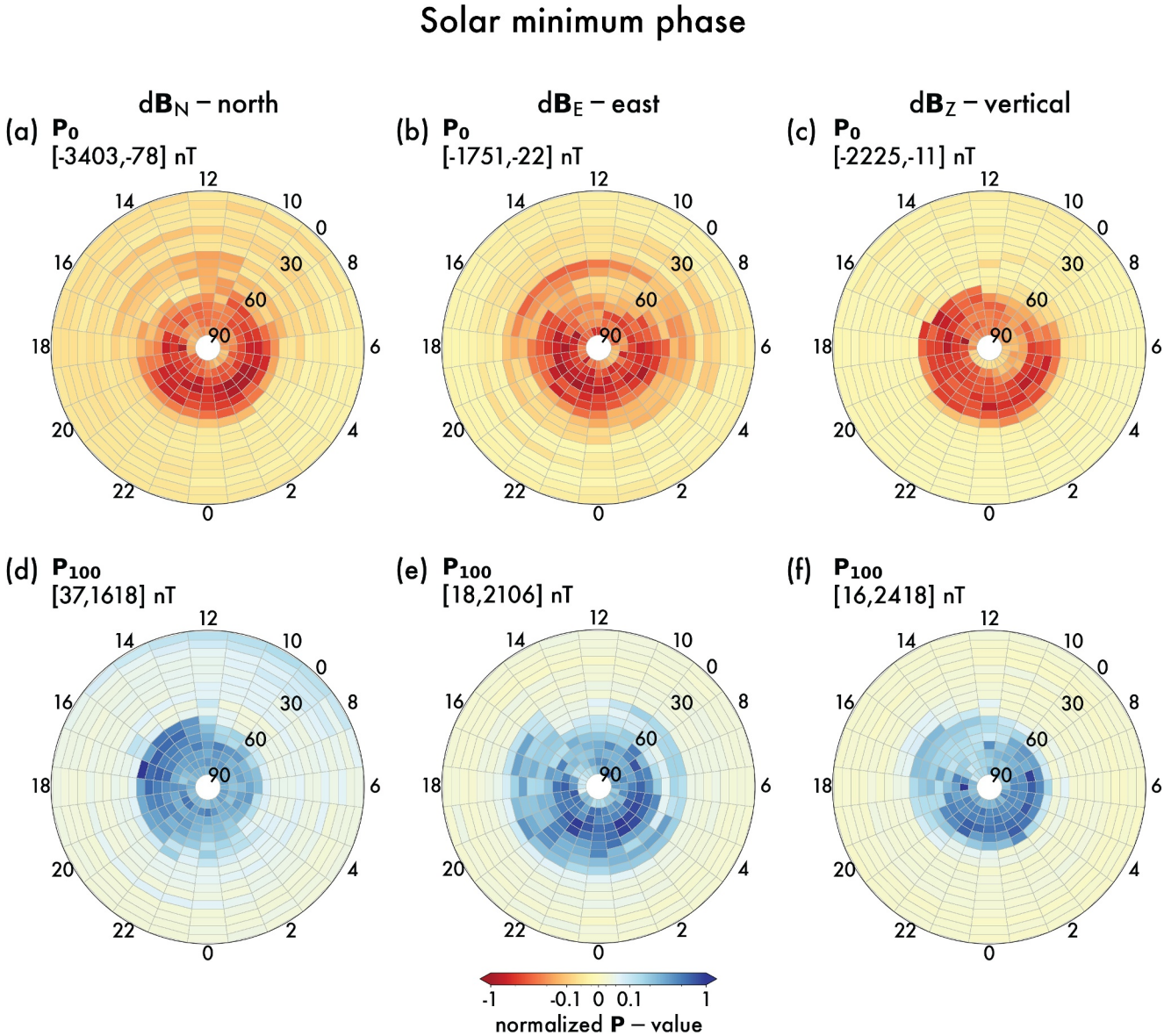

Figure 8. Percentile 0 ($\mathbf{P_0}$), "upper row" and percentile 100 ($\mathbf{P_{100}}$) "lower row" during the solar minimum phase.

study, Ohtani et al. (2023) addressed the external and internal causes of the stormtime intensification of the dawnside westward AEJ by tackling four main scenarios, the external driving of global convection, solar wind compression, formation of the substorm current wedge, and injection of energetic electrons by substorms. The results show that although the enhancement of external driving of global convection may precondition the AEJ intensification at dawn, it is rarely the direct cause, and that external compression probably explains only a small fraction of the events. Finally, the authors suggest that the substorm injection of energetic electrons might be the primary cause of this asymmetry. Evidence of this conclusion is based on the fact that the westward AEJ intensifies first around midnight, along with mid-latitude positive bays, before intensifying at dawn. It is worth noting, in light of these studies, that in addition to the intensification of the westward AEJ around midnight observed in our results in panels (a) of Figures 4 and 5, there is also an intensification of the perturbations in the east magnetic component in the midnight-dawn sector "see panel (e) of the same figures."

Figure 3 shows daytime perturbations in the north and east components ($\mathbf{dB_N}$ and $\mathbf{dB_E}$) at middle latitudes. These perturbations are associated with the Sq current system (e.g., Hasegawa, 1960; Pedatella et al., 2011). Although the median values of these perturbations are comparable to those at higher latitudes, very little activity is observed

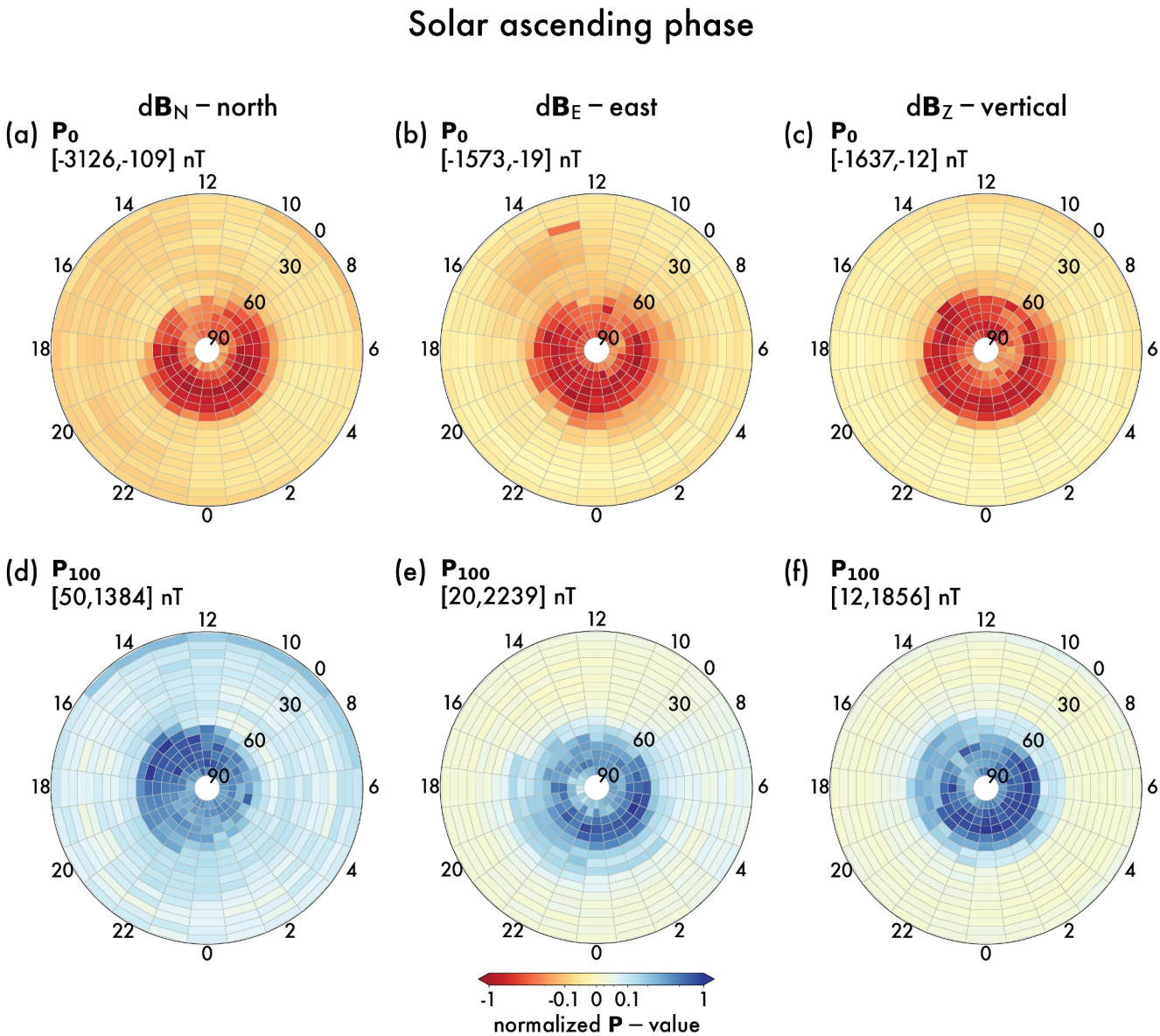

Figure 9. Percentile 0 ($\mathbf{P_0}$) "upper row" and percentile 100 ($\mathbf{P_{100}}$) "lower row" during solar ascending phase.

at middle latitudes for higher percentiles, as evidenced in Figure 4. At low latitudes, positive perturbations associated with the equatorial electrojet (EEJ) dominate the median values between 9 and 15 magnetic local times, as observed in the north component, $\mathbf{dB_N}$ "see panel (a) in Figure 3". This tendency for positive $\mathbf{dB_N}$ perturbations around noon remains consistent across the activity spectrum at the dip equator, as all the polar maps evidence. On the other hand, negative $\mathbf{B_N}$ perturbations dominate in the dusk-midnight sector at low and equatorial latitudes. These disturbances have a magnitude that exceeds that of positive disturbances by approximately threefold "see panels (a) and (d) in Figures 5–7." This prevalence of negative disturbances during periods of heightened geomagnetic activity at equatorial latitudes is supported by previous studies. Using ground magnetic records, Yamazaki and Kosch (2015) have statistically shown that as the geomagnetic activity increases, a westward disturbance EEJ starts to dominate in the daytime mainly due to the disturbance dynamo electric field, which occurs as a result of a change in the neutral winds convection and has been predicted to last for many hours after geomagnetic activity subsides. On the other hand, it is evident in Figure 7a, that negative perturbations in the north component concentrate mostly in the dusk sector. Newell and Gjerloev (2012) utilized the SuperMAG data repository to analyze the SuperMAG ring current index, SMR. As previously stated, this index is similar to DST or

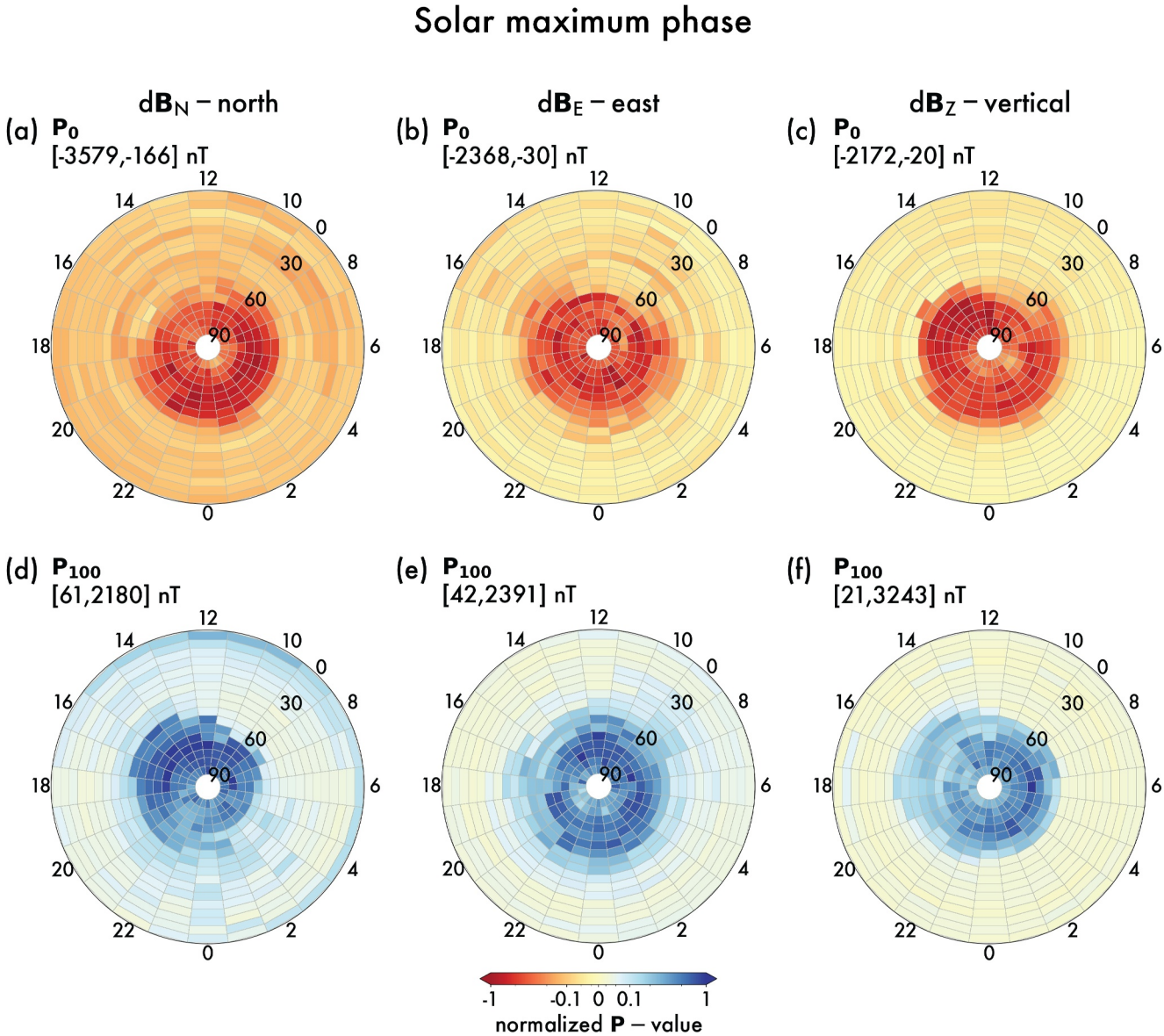

Figure 10. Percentile 0 ($\mathbf{P_0}$) "upper row" and percentile 100 ($\mathbf{P_{100}}$) "lower row" during solar maximum phase.

SYM-H but provides local time resolution from four sectors: midnight, dawn, noon, and dusk. The authors used a superposed epoch analysis to determine the average evolution of the SMR indices in the four local time sectors, using the start of the main phase (decrease of field strength) as the key time ($t = 0$). All four indices showed a southward deflection after onset but with different slopes. About 10 hr into the storm, minima were reached. The largest field depressions were found within the dusk sector, and the smallest around dawn. The difference in peak amplitude between dawn and dusk was approximately 30 nT. It is intriguing, however, why panel (a) of Figures 5–7 display larger negative perturbations in the north component around the dusk sector up to 10° of magnetic latitude only. Panel (b) of Figure 2 shows a decrease in the number of observations between 10° and 20° of magnetic latitude which might explain such observation.

The spatial patterns of geomagnetic perturbations (median values) seen in Figure 3 are observed to be less noticeable as perturbations intensify. This observation is characterized by very well-localized and randomly distributed perturbations, as shown in Figure 6. It is also apparent that this feature occurs differently at various latitudes. Figure 5 shows how the regular patterns start to vanish and localized perturbations show up at middle latitudes at $\mathbf{P_{0.001}}$ and $\mathbf{P_{99.999}}$ while at auroral regions the regular patterns are still fair to see. The absence of

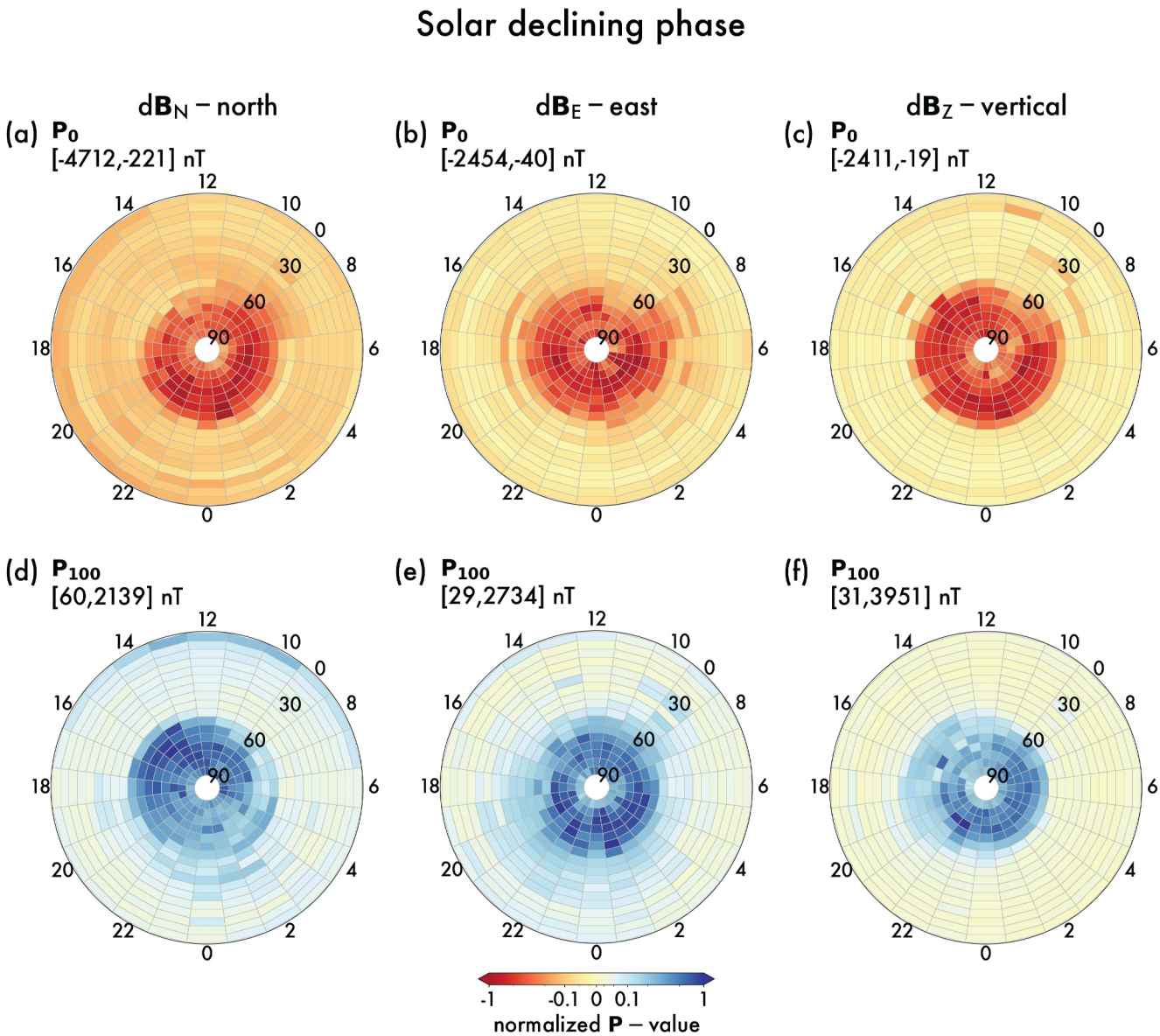

Figure 11. Percentile 0 ($\mathbf{P_0}$) "upper row" and percentile 100 ($\mathbf{P_{100}}$) "lower row" during solar descending phase.

evident patterns at middle latitudes can be explained by the nature of the Sq current. This current, responsible for the regular daily variation of the geomagnetic field on the order of a few tens of nano teslas, is primarily dependent on solar (local) time and is visible only when solar-wind-driven disturbances are absent. Geomagnetic disturbances associated with storms and substorms are usually several hundred nano teslas on the surface, which can easily mask underlying Sq signals (Yamazaki & Maute, 2017). It is worth mentioning as well, that R1-FACs might contribute to perturbations in the east magnetic component at middle latitudes by reducing the field strength.

At percentiles $\mathbf{P_{0.0001}}$ and $\mathbf{P_{99.9999}}$ when patterns in geomagnetic perturbations at auroral regions become indistinct, there are interesting observations about the vertical magnetic component $\mathbf{dB_Z}$ in panels (c) and (f) of Figures 6 and 7. Perturbations in this component are associated with the auroral electrojet (AEJ), similar to the north component $\mathbf{dB_N}$. However, disturbances in $\mathbf{dB_Z}$ do not exhibit the same preference in local time as $\mathbf{dB_N}$. This observation is more pronounced in the negative $\mathbf{dB_Z}$ perturbations, which are almost uniformly present at all local times. In a study about ground geomagnetic perturbations under different interplanetary magnetic field conditions, D. Weimer et al. (2010) highlighted a notable correlation between the vertical component of magnetic

perturbations and the observed patterns of field-aligned currents (FAC) derived from satellite magnetic records. The authors explain that in the auroral zone, FAC sheets manifest where electric fields diverge or converge. Consequently, ionospheric Hall currents on opposite sides of the divergence exhibit opposite polarities. Applying the "right-hand rule," it becomes apparent that a vertical magnetic perturbation arises beneath the point where the Hall currents change polarity. Nevertheless, the relationship between FAC magnitudes and vertical perturbations would depend on the ratio of Hall and Pedersen conductivities, as well as the profiles of electric fields.

After analyzing magnetic records from 1976 to 2023 and categorizing them into four solar phases (minimum, ascending, maximum, and declining), it is clear that the strongest disturbances occur during the solar declining phase, while the weakest occur during the ascending phase. This finding is consistent with previous research which demonstrated that the lowest geomagnetic activity typically takes place just after the minimum in sunspot numbers, while the highest activity occurs during the declining phase of each solar cycle (Hathaway, 2015). It is important to note that the most severe disturbances are associated with the westward auroral electrojet AEJ in the midnight-dawn sector, which is characterized by negative $\mathbf{dB_N}$. This observation holds during all four solar phases when comparing these disturbances with the other two magnetic components $\mathbf{dB_E}$ and $\mathbf{dB_Z}$. Additionally, it is interesting to note that although the spatial patterns in geomagnetic disturbances become less recognizable around percentiles 0.0001 and 99.9999, during the solar ascending phase, such patterns tend to hold better at those percentiles than during the other three solar phases.

5. Conclusions

In this study, we utilize ground magnetic records from the extensive multi-year data set provided by the SuperMAG collaboration from 1976 to 2023 to comprehensively examine geomagnetic perturbations separately in the three magnetic components. We analyze their dependence on magnetic latitude and local time, covering low, middle, and high magnetic latitudes in the northern hemisphere, where the largest and oldest data sets are available. Our principal aim is to quantify extreme values and evaluate their variability on magnetic latitude, local time, and solar cycle phases. This was achieved by analyzing various percentiles as a function of magnetic latitude and magnetic local time and comparing the results for percentiles close to extreme values during four different solar phases (minimum, ascending, maximum, and declining).

The key findings of this study are as follows:

1. Median values of geomagnetic perturbations show coherent spatial patterns in the order of tens of nanoteslas that can be explained in terms of field-aligned currents, auroral and equatorial electrojets, and Sq currents.
2. At the auroral region, the patterns shift equatorward as the intensity of the perturbations increases. The coherence of the patterns prevails until they become indistinct about percentiles 0.0001 and 99.9999 ($\mathbf{P_{0.0001}}$ and $\mathbf{P_{99.9999}}$).
3. Perturbations associated with the auroral electrojets (AEJ) show an apparent dusk-dawn asymmetry with values of the westward AEJ at the dawn doubling those of its dusk counterpart. This observation is aligned with a recent study that argues that the substorm injection of energetic electrons might be the primary cause of this asymmetry (Ohtani et al., 2023).
4. At middle latitudes, coherent patterns related to Sq currents get masked around percentiles 0.001 and 99.999 ($\mathbf{P_{0.001}}$ and $\mathbf{P_{99.999}}$). This early fadeaway of the patterns compared to the auroral zone might be related to geomagnetic perturbations associated with storms which are several hundred nano teslas on the surface and can easily mask underlying Sq signals.
5. It has been noticed that extreme values occur in specific regions based on magnetic latitude and local time. The north magnetic component shows a tendency toward positive perturbations in the noon-dusk sector and negative ones in the midnight-dawn sector. However, the east and vertical magnetic components display localized extreme values that are randomly distributed.
6. Upon comparing geomagnetic perturbations near extreme values ($\mathbf{P_{0.0001}}$ and $\mathbf{P_{99.9999}}$), it becomes clear that the most intense perturbations occur primarily during the solar declining phase while the weakest occur during the solar ascending phase. Furthermore, it was observed that the strongest perturbations are linked with the westward auroral electrojet, independently of the solar phase cycle.

Finally, our study sheds light on the complex dynamics of geomagnetic perturbations and their variations with magnetic latitude, local time, and solar phase cycle. Our findings highlight the importance of understanding their spatial patterns for space weather forecasting and mitigation strategies. Specifically, the observed asymmetries in

auroral electrojets and the association of extreme perturbations with the solar declining phase provide valuable insights for improving our ability to predict and prepare for space weather events. This study underscores the critical role of long-term, comprehensive observations in advancing our understanding of space weather phenomena and their impacts on technological infrastructure and society.

Data Availability Statement

Magnetic records are available on the SuperMAG website (https://supermag.jhuapl.edu/mag).

Acknowledgments
All magnetic records used in this study are accessible on the SuperMAG website (http://supermag.jhuapl.edu/mag). SuperMAG is an international collaboration of multiple organizations and institutes (https://supermag.jhuapl.edu/contrib/) funded by the National Science Foundation (NSF). JRZ and SO received support from NSF Grant 2224986 and NASA Grant 80NSSC21K003. Additionally, JRZ was also supported through NSF PREEVENTS award 1663885.

References

Baker, D. N., Li, X., Pulkkinen, A., Ngwira, C., Mays, M., Galvin, A., & Simunac, K. (2013). A major solar eruptive event in july 2012: Defining extreme space weather scenarios. *Space Weather*, *11*(10), 585–591. https://doi.org/10.1002/swe.20097

Baumjohann, W. (1982). Ionospheric and field-aligned current systems in the auroral zone: A concise review. *Advances in Space Research*, *2*(10), 55–62. https://doi.org/10.1016/0273-1177(82)90363-5

Bergin, A., Chapman, S. C., Watkins, N. W., Moloney, N. R., & Gjerloev, J. W. (2023). Extreme event statistics in dst, sym-h, and smr geomagnetic indices. *Space Weather*, *21*(3), e2022SW003304. https://doi.org/10.1029/2022sw003304

Cliver, E. W., & Svalgaard, L. (2004). The 1859 solar–terrestrial disturbance and the current limits of extreme space weather activity. *Solar Physics*, *224*(1–2), 407–422. https://doi.org/10.1007/s11207-005-4980-z

Getachew, T., Virtanen, I., & Mursula, K. (2017). Structure of the photospheric magnetic field during sector crossings of the heliospheric magnetic field. *Solar Physics*, *292*(11), 1–19. https://doi.org/10.1007/s11207-017-1198-9

Gjerloev, J. (2012). The supermag data processing technique. *Journal of Geophysical Research*, *117*(A9). https://doi.org/10.1029/2012ja017683

Hasegawa, M. (1960). On the position of the focus of the geomagnetic sq current system. *Journal of Geophysical Research*, *65*(5), 1437–1447. https://doi.org/10.1029/jz065i005p01437

Hathaway, D. H. (2015). The solar cycle. *Living Reviews in Solar Physics*, *12*(1), 4. https://doi.org/10.1007/lrsp-2015-4

Iijima, T., & Potemra, T. A. (1976). Field-aligned currents in the dayside cusp observed by triad. *Journal of Geophysical Research*, *81*(34), 5971–5979. https://doi.org/10.1029/ja081i034p05971

Juusola, L., Kauristie, K., Vanhamäki, H., Aikio, A., & Van De Kamp, M. (2016). Comparison of auroral ionospheric and field-aligned currents derived from swarm and ground magnetic field measurements. *Journal of Geophysical Research: Space Physics*, *121*(9), 9256–9283. https://doi.org/10.1002/2016ja022961

Kamide, Y., Richmond, A., & Matsushita, S. (1981). Estimation of ionospheric electric fields, ionospheric currents, and field-aligned currents from ground magnetic records. *Journal of Geophysical Research*, *86*(A2), 801–813. https://doi.org/10.1029/ja086ia02p00801

Kilpua, E., Olspert, N., Grigorievskiy, A., Käpylä, M., Tanskanen, E., Miyahara, H., et al. (2015). Statistical study of strong and extreme geomagnetic disturbances and solar cycle characteristics. *The Astrophysical Journal*, *806*(2), 272. https://doi.org/10.1088/0004-637x/806/2/272

Koons, H. (2001). Statistical analysis of extreme values in space science. *Journal of Geophysical Research*, *106*(A6), 10915–10921. https://doi.org/10.1029/2000ja000234

Lanzerotti, L. J. (2017). Space weather: Historical and contemporary perspectives. *Space Science Reviews*, *212*(3–4), 1253–1270. https://doi.org/10.1007/s11214-017-0408-y

Legrand, J., & Simon, P. (1989). Solar cycle and geomagnetic activity: A review for geophysicists. Part i. The contributions to geomagnetic activity. *Annales Geophysicae*, *7*, 565–578.

Love, J. J., Rigler, E. J., Pulkkinen, A., & Riley, P. (2015). On the lognormality of historical magnetic storm intensity statistics: Implications for extreme-event probabilities. *Geophysical Research Letters*, *42*(16), 6544–6553. https://doi.org/10.1002/2015gl064842

Lühr, H., Alken, P., & Zhou, Y.-L. (2021). The equatorial electrojet. *Ionosphere Dynamics and Applications*, 281–299. https://doi.org/10.1002/9781119815617.ch12

Newell, P., & Gjerloev, J. (2011). Evaluation of supermag auroral electrojet indices as indicators of substorms and auroral power. *Journal of Geophysical Research*, *116*(A12). https://doi.org/10.1029/2011ja016779

Newell, P., & Gjerloev, J. (2012). Supermag-based partial ring current indices. *Journal of Geophysical Research*, *117*(A5). https://doi.org/10.1029/2012ja017586

Ohtani, S. (2021). Revisiting the partial ring current model: Longitudinal asymmetry of ground magnetic depression during geomagnetic storms. *Journal of Geophysical Research: Space Physics*, *126*(9), e2021JA029643. https://doi.org/10.1029/2021ja029643

Ohtani, S., Sorathia, K., Merkin, V., Frey, H., & Gjerloev, J. (2023). External and internal causes of the stormtime intensification of the dawnside westward auroral electrojet. *Journal of Geophysical Research: Space Physics*, *128*(10), e2023JA031457. https://doi.org/10.1029/2023ja031457

Pedatella, N., Forbes, J., & Richmond, A. (2011). Seasonal and longitudinal variations of the solar quiet (sq) current system during solar minimum determined by champ satellite magnetic field observations. *Journal of Geophysical Research*, *116*(A4). https://doi.org/10.1029/2010ja016289

Pulkkinen, A., Kuznetsova, M., Ridley, A., Raeder, J., Vapirev, A., Weimer, D., et al. (2011). Geospace environment modeling 2008–2009 challenge: Ground magnetic field perturbations. *Space Weather*, *9*(2). https://doi.org/10.1029/2010sw000600

Reyes, P. I., Pinto, V. A., & Moya, P. S. (2021). Geomagnetic storm occurrence and their relation with solar cycle phases. *Space Weather*, *19*(9), e2021SW002766. https://doi.org/10.1029/2021sw002766

Riley, P. (2018). Statistics of extreme space weather events. In N. Buzulukova (Ed.), *Extreme events in geospace* (pp. 115–138). Elsevier. https://doi.org/10.1016/B978-0-12-812700-1.00005-4

Riley, P., & Love, J. J. (2017). Extreme geomagnetic storms: Probabilistic forecasts and their uncertainties. *Space Weather*, *15*(1), 53–64. https://doi.org/10.1002/2016sw001470

Takeda, M. (1999). Time variation of global geomagnetic sq field in 1964 and 1980. *Journal of Atmospheric and Solar-Terrestrial Physics*, *61*(10), 765–774. https://doi.org/10.1016/s1364-6826(99)00028-0

Tsubouchi, K., & Omura, Y. (2007). Long-term occurrence probabilities of intense geomagnetic storm events. *Space Weather*, *5*(12). https://doi.org/10.1029/2007sw000329

Weimer, D. (2001). Maps of ionospheric field-aligned currents as a function of the interplanetary magnetic field derived from dynamics explorer 2 data. *Journal of Geophysical Research*, *106*(A7), 12889–12902. https://doi.org/10.1029/2000ja000295

Weimer, D., Clauer, C., Engebretson, M., Hansen, T., Gleisner, H., Mann, I., & Yumoto, K. (2010). Statistical maps of geomagnetic perturbations as a function of the interplanetary magnetic field. *Journal of Geophysical Research*, *115*(A10). https://doi.org/10.1029/2010ja015540

Weimer, D. R. (2013). An empirical model of ground-level geomagnetic perturbations. *Space Weather*, *11*(3), 107–120. https://doi.org/10.1002/swe.20030

Woodroffe, J. R., Morley, S., Jordanova, V., Henderson, M., Cowee, M., & Gjerloev, J. (2016). The latitudinal variation of geoelectromagnetic disturbances during large (dst ≤ - 100 nt) geomagnetic storms. *Space Weather*, *14*(9), 668–681. https://doi.org/10.1002/2016sw001376

Xiong, C., Stolle, C., Alken, P., & Rauberg, J. (2020). Relationship between large-scale ionospheric field-aligned currents and electron/ion precipitations: Dmsp observations. *Earth Planets and Space*, *72*(1), 1–22. https://doi.org/10.1186/s40623-020-01286-z

Yamazaki, Y., & Kosch, M. J. (2015). The equatorial electrojet during geomagnetic storms and substorms. *Journal of Geophysical Research: Space Physics*, *120*(3), 2276–2287. https://doi.org/10.1002/2014ja020773

Yamazaki, Y., & Maute, A. (2017). Sq and eej—A review on the daily variation of the geomagnetic field caused by ionospheric dynamo currents. *Space Science Reviews*, *206*(1–4), 299–405. https://doi.org/10.1007/s11214-016-0282-z